

STELLAR METALLICITY OF THE EXTENDED DISK AND DISTANCE OF THE SPIRAL GALAXY NGC 3621

ROLF-PETER KUDRITZKI¹

Institute for Astronomy, University of Hawaii, 2680 Woodlawn Drive, Honolulu, HI 96822, USA

MIGUEL A. URBANEJA

Institute for Astro- and Particle Physics, University of Innsbruck, Technikerstr. 25/8, A-6020 Innsbruck, Austria

FABIO BRESOLIN

Institute for Astronomy, University of Hawaii, 2680 Woodlawn Drive, Honolulu, HI 96822, USA

MATTHEW W. HOSEK JR.

Institute for Astronomy, University of Hawaii, 2680 Woodlawn Drive, Honolulu, HI 96822, USA

AND

NORBERT PRZYBILLA

Institute for Astro- and Particle Physics, University of Innsbruck, Technikerstr. 25/8, A-6020 Innsbruck, Austria
To appear in Astrophysical Journal

ABSTRACT

Low resolution ($\sim 4.5 \text{ \AA}$) ESO VLT/FORS spectra of blue supergiant stars are analyzed to determine stellar metallicities (based on elements such as iron, titanium, magnesium) in the extended disk of the spiral galaxy NGC 3621. Mildly subsolar metallicity (-0.30 dex) is found for the outer objects beyond 7 kpc independent of galactocentric radius and compatible with the absence of a metallicity gradient confirming the results of a recent investigation of interstellar medium H II region gas oxygen abundances. The stellar metallicities are slightly higher than those from the H II regions when based on measurements of the weak forbidden auroral oxygen line at 4363 \AA but lower than the ones obtained with the R_{23} strong line method. It is shown that the present level of metallicity in the extended disk cannot be the result of chemical evolution over the age of the disk with the present rate of in situ star formation. Additional mechanisms must be involved. In addition to metallicity, stellar effective temperatures, gravities, interstellar reddening, and bolometric magnitudes are determined. After application of individual reddening corrections for each target the flux-weighted gravity-luminosity relationship of blue supergiant stars is used to obtain a distance modulus of $29.07 \pm 0.09 \text{ mag}$ (distance $D = 6.52 \pm 0.28 \text{ Mpc}$). This new distance is discussed in relation to Cepheid and tip of the red giant branch distances.

Subject headings: galaxies: distances and redshifts — galaxies: individual(NGC 3621) — stars: abundances — stars: early-type — supergiants

1. INTRODUCTION

NGC 3621 is a bulgeless isolated galaxy with a relatively regular spiral structure which extends out to at least two isophotal radii. The galaxy with its extended disk is imbedded into an envelope of neutral hydrogen gas (Koribalski et al. 2004). A recent study by Bresolin et al. (2012) analyzing the emission lines of H II region spectra reveals that the extended disk (beyond 0.8 isophotal radii) has no oxygen abundance gradient and shows an oxygen abundance distribution which is spatially flat at a relatively high level of -0.4 dex below solar oxygen abundance. While the flatness, though striking, does not seem to be a major issue and according to Bresolin et al. can be explained by the fact that the star formation efficiency is almost constant with radius in the extended disk, it is the

high level of metallicity which poses a problem. Bresolin et al. estimate that with the large neutral hydrogen gas reservoir and the low-level of ongoing star formation the time required to enrich the interstellar gas to the observed level is 10 Gyr. While inner disks may have such an age, Bresolin et al. argue that outer disks are at least a factor of two younger. Thus, chemical enrichment of the interstellar medium through in situ star formation at the present level could have resulted only in a very low oxygen abundance with values smaller than -0.7 dex below the solar abundance. As possible mechanisms to explain the discrepancy Bresolin et al. discuss radial metal transport from the inner to the outer disk and gas accretion from the intergalactic medium by metal enriched galactic outflows.

There are many galaxies with extended star forming disks and a flat oxygen abundance distribution, for instance M83 (Bresolin et al. 2009b), NGC 4624 (Goddard et al. 2011), NGC 1512 (Bresolin et al. 2012) and the thirteen mostly merging galaxies investigated by Werk et al. (2011). However, NGC 3621 appears to be the poster example for a galaxy with a well defined inner abundance gradient and a large outer extended disk with a flat metallicity distribution (see Figure 9

kud@ifa.hawaii.edu
Miguel.Urbaneja-Perez@uibk.ac.at
bresolin@ifa.hawaii.edu
mwhosek@ifa.hawaii.edu
Norbert.Przybilla@uibk.ac.at
Miguel.Urbaneja-Perez@uibk.ac.at

¹University Observatory Munich, Scheinerstr. 1, D-81679 Munich, Germany

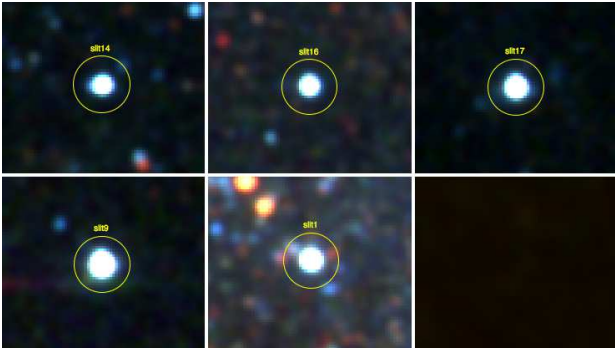


FIG. 1.— Enlarged B, V, I composite HST ACS images of five of the observed BSG targets. The circle corresponds to 1 arcsec diameter.

of Bresolin et al. 2012). In addition, NGC 3621 is also the case where the discrepancy between expected and observed outer disk metallicity, as discussed above, is most significant. We have, thus, decided to reinvestigate the metallicity distribution in the disk of this galaxy using an independent alternative method, the spectral analysis of blue supergiant stars (BSGs). With absolute magnitudes up to $M_V \cong -10$ BSGs are the brightest star in the universe at visual light and perfect objects for quantitative stellar abundance studies beyond the Local Group. They are massive stars in the range between 15 and $40 M_\odot$. At an age of ~ 10 million years they have left the main sequence and cross the Hertzsprung-Russell diagram to become red supergiant stars and then to explode as core collapse supernovae. Kudritzki et al. (2008) in their study of metallicity in the Sculptor spiral galaxy NGC 300 were the first to demonstrate how accurate metallicities based on elements such as iron, chromium, titanium etc. can be determined from low resolution spectra of individual BSGs using model atmosphere techniques. Since then a large number of galaxies has been studied (WLM – Bresolin et al. 2006; Urbaneja et al. 2008; NGC 3109 – Evans et al. 2007, Hosek et al. 2014; IC 1613 – Bresolin et al. 2007; M33 – U et al. 2009; NGC 55 – Castro et al. 2012; M81 – Kudritzki et al. 2012; NGC 4258 – Kudritzki et al. 2013).

A particular motivation for this work is the systematic uncertainty inherent in H II region abundance studies. In most cases they are based on the use of the strongest nebular emission lines and using oxygen as a proxy for stellar metallicity. However, as shown, for instance, by Kudritzki et al. (2008), Kewley & Ellison (2008), Bresolin et al. (2009a), U et al. (2009), Kudritzki et al. (2012) these “strong-line methods” are subject to systematic uncertainties as large as 0.6 dex. They are poorly understood and can severely affect the values of galaxy metallicities and abundance gradients. Bresolin et al. (2012) were aware of this uncertainty in their investigation of NGC 3621 and used three different strong line calibrations. They all resulted in a flat oxygen abundance distribution over the outer extended disk, however the abundance level was different. Two calibrations yielded -0.44 dex lower than solar, whereas the third showed a much higher value, only -0.08 dex below and, thus, almost solar. In addition to the calibration dependent use of strong lines Bresolin et al. (2012) were also able to determine H II region electron temperatures from the detection of the weak auroral [OIII] 4363 line, which was detected in 12 of the observed 72 H II regions. Nebular oxygen abundance determinations based on the temperature information of this line are more reliable, as it can be used to calculate the excitation of the upper levels

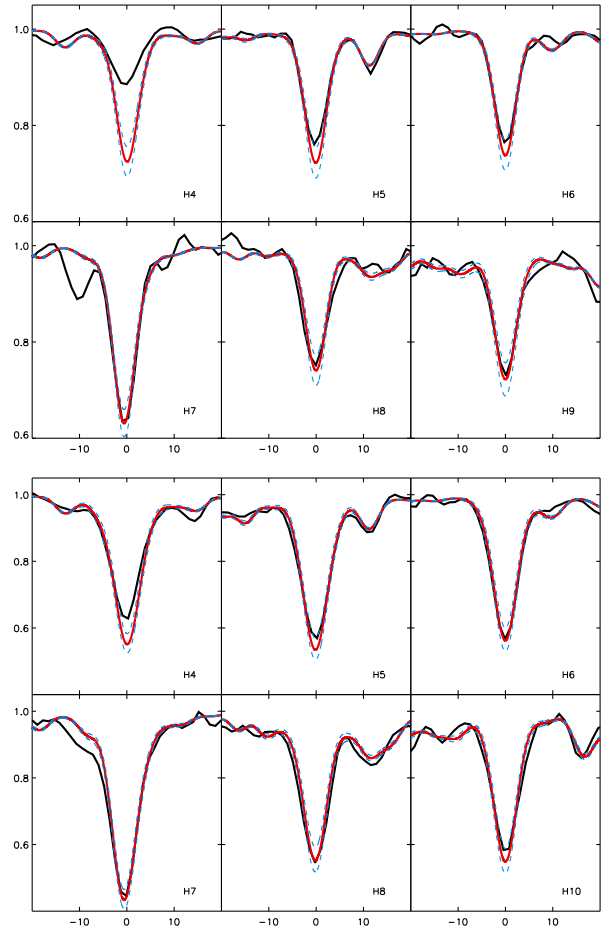


FIG. 2.— Top: Fit of observed Balmer line profiles (black solid) of target Slit 9 with model atmospheres of $T_{\text{eff}}=8750\text{K}$ and $\log g = 1.00$ (red, solid) and 0.95 and 1.05 (both blue dashed), respectively. Bottom: Similar fit of target Slit 17 with $T_{\text{eff}}=8100\text{K}$ and $\log g =0.90$ (red, solid) and 0.85, 0.95 (blue dashed). The gravities $\log g$ are given in cgs units.

of the strong lines and thus their emission coefficient. For instance, in the case of the galaxy NGC 300 excellent agreement has been found by Bresolin et al. (2009a) between H II region and BSG metallicities. On the other hand, the work by Stasińska (2005), Bresolin et al. (2005), Ercolano et al. (2010), and Zurita & Bresolin (2012) indicates that also this method might be subject to uncertainties albeit much smaller than the strong line methods. An additional, more general problem of the oxygen abundances obtained from H II regions might be the depletion of oxygen through the formation of dust grains (for a discussion see Bresolin et al. 2009a). While the BSG abundance determination may certainly also be subject to systematic uncertainties, we see a double advantage in the investigation of BSG metallicities in the disk of NGC 3621. First, it simply provides an independent measurement of metallicity using a well established accurate method. Second, it will give information about metallicity from elements other than oxygen and more relevant to “metallicity” in the sense of chemical evolution. We hope to use this advantage to develop improved constraints on the metallicity enrichment of the outer disks of star forming galaxies.

NGC 3621 is not only interesting with regard to disk evolution and star formation. It is also an important galaxy for the determination of extragalactic distance scale. With an incli-

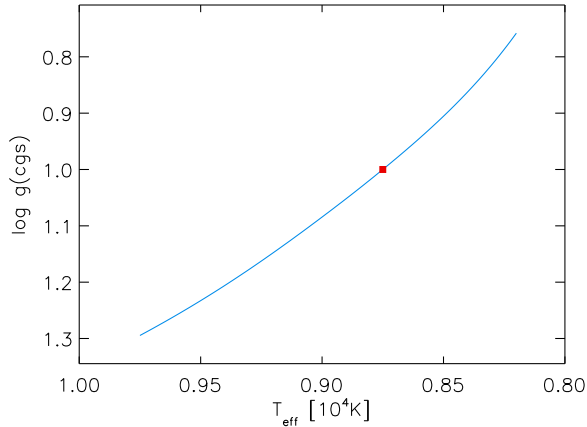


FIG. 3.— Fit curve in the gravity-temperature plane for target Slit 9 along which the calculated Balmer line profiles agree with the observations. The fit point of Figure 2 (top) is indicated by the red square.

nation angle of 65 degrees (de Blok et al. 2008) and well ordered H I rotation it is an ideal galaxy for the calibration of the Tully-Fisher method. It is, thus, not surprising that it has been included in the Hubble Space Telescope Extragalactic Distance Scale Key Project (Freedman et al. 2001). Also the HST tip of the red giant branch (TRGB) study to calibrate type I supernovae as distance indicators by Mould & Sakai (2008) has included this important galaxy. Distance moduli determined over the last 13 years vary between 28.9 and 29.4 mag (see NED database <http://ned.ipac.caltech.edu>). Our BSG spectroscopic study provides an important alternative for distance determination through the use of the flux-weighted gravity – luminosity relationship (FGLR). This technique, which uses the determination of stellar temperature and gravities to predict absolute bolometric magnitudes, has been introduced by Kudritzki et al. (2003) and Kudritzki et al. (2008) and has already been applied successfully in a variety of cases (WLM – Urbaneja et al. 2008; NGC 3109 – Hosek et al. 2014; M33 – U et al. 2009; M81 – Kudritzki et al. 2012).

2. TARGET STARS AND OBSERVATIONS

The observations of the BSG target stars were carried out in 2000 March 1-2 with the focal reducer low-dispersion spectrograph FORS1 attached to the ESO VLT and are described in detail in Bresolin, Kudritzki, Mendez & Pryzibilla (2001, hereinafter BKMP). In summary, several exposures of one single multislit setup were taken with a total integration time of 10.7 hours using a 600 groove/mm grism and slitlets with a width of 1 arcsecond. The spectra cover a range of 3700 to 5000 Å. The nominal resolution is 5 Å, however, with 0.8 arcsec seeing conditions the effective resolution obtained was slightly higher. For the quantitative spectral analysis described in the next section the spectra were box smoothed over three pixel (1 pixel corresponds to 1.195 Å). After smoothing the spectral resolution measured was about 4.5 Å. The signal-to-noise ratio of the smoothed spectra varies between 120 and 45 depending on the brightness of the objects and how well they were centered into the slitlets.

The observations were part of the FORS Guaranteed Time Observing (GTO) program and were thought as a pilot study to demonstrate the feasibility of spectroscopy of individual supergiant stars in galaxies at distances significantly beyond the Local Group. When the observed spectra were presented

TABLE 1
NGC 3621 - SPECTROSCOPIC TARGETS

name ^a	α_{2000} ^a h min sec	δ_{2000} ^a ° ' ''	R/R ₂₅ ^b	sp.t.	m _V mag	B-V mag	V-I mag	S
(1)	(2)	(3)	(4)	(5)	(6)	(7)	(8)	(9)
Slit 1	11 18 14.3	-32 45 40.1	0.68	A1	21.236	0.240	0.282	5
Slit 3 ^c	11 18 10.3	-32 45 31.4	0.63	B5	21.573	0.084	0.199	4
Slit 9	11 18 28.7	-32 48 04.6	1.29	A2	20.390	0.244	0.294	1
Slit 14	11 18 26.6	-32 50 05.8	0.91	A4	21.859	0.267	0.326	4
Slit 16	11 18 23.3	-32 51 02.7	0.64	B9	21.594	0.172	0.174	5
Slit 17	11 18 27.5	-32 51 05.4	0.98	A5	20.888	0.289	0.320	8

^a Bresolin et al. (2012)

^b Galactocentric distance, in units of R₂₅ = 4.89 arcmin \approx 9.28 kpc (distance modulus 29.07 mag).

A position angle PA = 345°, an inclination $i = 65^\circ$ and central coordinates $\alpha_{2000} = 11\text{h}18\text{m}16.52\text{sec}$,

$\delta_{2000} = -32^\circ48'50.7''$ were assumed (Hyperleada data base, Paturel et al., 2003)

^c no HST photometry, see text

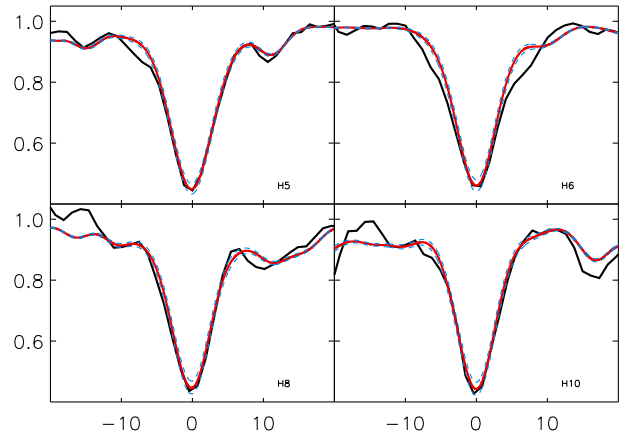


FIG. 4.— Fit of observed Balmer line profiles (black solid) of target Slit 14 with model atmospheres of $T_{\text{eff}} = 8300\text{K}$ and $\log g = 1.25$ (red, solid) and 1.20 and 1.30 (both blue dashed), respectively.

in BKMP, the method for a consistent quantitative analysis based on model atmospheres of the low resolution spectra still had to be developed. As a first step, BKMP determined spectral types. For one supergiant target of spectral type A (Slit 9) they used the spectral type to estimate effective temperature and calculated model atmospheres at this temperature to qualitatively estimate metallicity. LMC metallicity was found for this target.

However, Evans & Howarth (2003) correctly pointed out that because the relationship between spectral type and effective temperature is metallicity dependent the uncertainties introduced in this way can be significant. Thus, a new method was needed providing a self-consistent determination of temperatures, gravities and metallicities. Such a method was developed by Kudritzki et al. (2008) in their work on BSGs in the Sculptor galaxy NGC 300 and further improved in the subsequent papers referred to in the previous section. The application of this new method on the old FORS spectra of the year 2000 enables us now to resume the quantitative spectroscopic study originally intended.

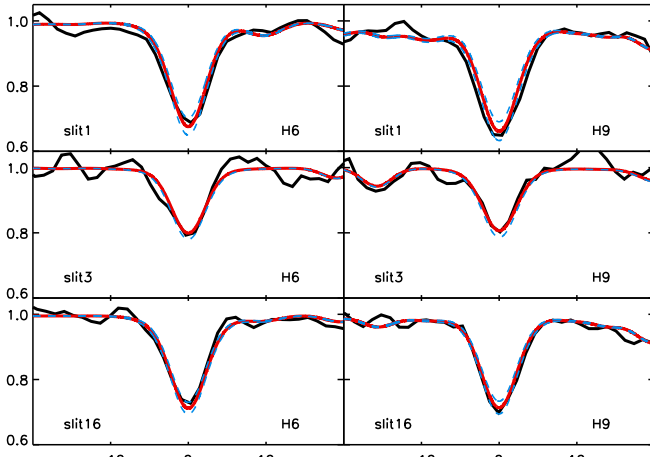


FIG. 5.— Fit of observed Balmer line profiles H_6 and H_9 of targets Slit 1, 3, and 16 (black solid). The model atmospheres (red, solid) used are $T_{eff}=9000\text{K}$, $\log g = 1.20$ for Slit 1, $T_{eff}=13500\text{K}$, $\log g = 1.70$ for Slit 3 and $T_{eff}=10500\text{K}$, $\log g = 1.50$ for Slit 16. Additional models with $\log g$ 0.05 dex smaller or larger are plotted as blue-dashed.

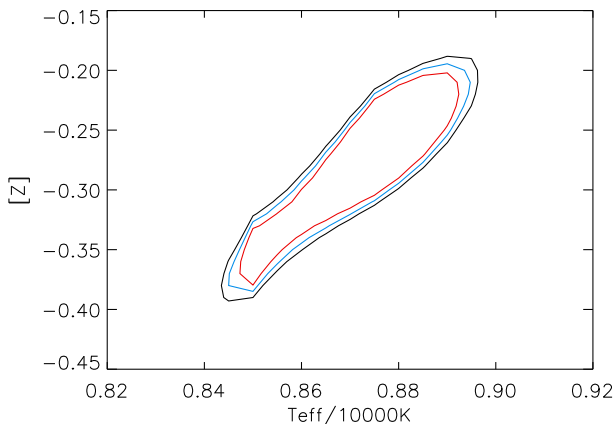


FIG. 6.— Isocontours $\Delta\chi^2$ for target Slit 9 in the metallicity $[Z]$ and effective temperature T_{eff} plane obtained from the fit of metal lines. $\Delta\chi^2=3$ (red), 6 (blue), 9 (black), respectively, are plotted.

18 stellar targets were originally selected by BKMP from broad-band color magnitude diagrams (B, V, I CCD frames taken with VLT/FORS) after careful inspection of the ground-based images ($\text{FWHM} \approx 0.6$ arcsec) with respect to blending with other sources. They were then observed with the single multislit setup. Of these 18 targets eight showed spectra of isolated individual BSGs. The other objects were either emission line stars with spectra resembling luminous blue variables (LBV) or displayed composite spectra or very strong ISM nebular emission contaminating the stellar absorption lines. Seven of the BSGs had the right spectral type A or B for which our model atmosphere analysis method is applicable. Unfortunately, for one of these BSGs the signal to noise ratio of the observed spectrum turned out to be insufficient for a spectral analysis. Thus, we were left with six BSG objects for our spectroscopic study. The observed properties of these objects are given in Table 1. Their location within NGC 3621 is shown in Figure 1 of BKMP.

NGC 3621 has also been studied with HST/ACS (HST-GO-9492, P.I.: Fabio Bresolin) in three filters, F435W, F555W, and F814W. Two ACS fields are available which include five of our six targets. PSF-photometry of the stellar sources was carried out of all the individual uncombined bias subtracted, flat-fielded images available from the STScI archive. The ACS module included in the DOLPHOT software package (Dolphin et al. 2002) was used together with a drizzle image for each pointing as a reference frame corresponding to the F555W filter. ACS/DOLPHOT can be applied with a variation of a large set of parameters. Here, the parameter values of the ANGST survey (Dalcanton et al. 2009) were replicated and used. The magnitudes obtained in the ACS filter system were then transformed to the Johnson-Cousins system. B, V, I magnitudes are given in Table 1. Object Slit 3 of Table 1 is not covered by the HST observations and only ground based BVI photometry published by BKMP is available. On the other hand, for ten targets of BKMP listed in their Table 1 we were able to obtain HST/ACS photometry allowing us to apply a transformation of BKMP to HST/ACS photometry for Slit 3. With magnitude differences between HST and FORS $\Delta m = -0.013, -0.097$ and -0.126 mag for B, V, and I, respectively, we obtain the photometric values for Slit 3 in Table 1.

Figure 1 shows enlarged B, V, I composite images of the five targets observed with HST/ACS and demonstrate that the selection based on high quality FORS images worked well. The targets are fairly isolated. For each of them the brightest neighbor object within a box of one arcsec diameter is at least three magnitudes fainter.

In their distribution of galactocentric distance the BSGs studied cover the range from 0.6 to 1.3 in R/R_{25} (R_{25} is the isophotal radius, see Table 1). According to Bresolin et al. (2012) (see their Figure 9) this is the range in galactocentric distance where the metallicity gradient of the inner disk flattens and the metallicity distribution becomes constant (see also figure 13). At the same time, the targets cover a range of one magnitude in brightness sufficient for an application of the FGLR-method to determine a distance.

3. SPECTROSCOPIC ANALYSIS

The goal of the spectroscopic analysis is the determination of stellar effective temperature, gravity and metallicity for our BSG targets. For this purpose we compare the normalized observed spectra with synthetic spectra of a comprehensive grid of line-blanketed model atmospheres and detailed NLTE line formation calculations. The grid of model spectra and the analysis method are described in Kudritzki et al. (2008, 2012, 2013) and Hosek et al. (2014). The analysis progresses in several steps. The first step is the fit of the Balmer lines. We estimate an effective temperature T_{eff} from the spectral type and determine the gravity $\log g$ at which we obtain the best fit of the Balmer lines. An example is given in Figure 2 for targets Slit 9 and 17. The comparison of the different higher Balmer lines $H_{6,7,8,9,10}$ indicates that a fit of $\log g$ accurate to 0.05 dex or better is possible at a fixed temperature T_{eff} . H_4 is often contaminated by stellar wind and H II region emission. The effect is clearly present in the examples of figure 2. In cases of very strong stellar winds and H II emission this can also affect H_5 (see figure 2) and H_6 (Slit 9 in figure 2). H_7 can sometimes be blended by interstellar CaII depending on the strength of interstellar absorption (the blend by stellar CaII is included in the model atmosphere calculations).

The strengths of the Balmer lines does not only depend on gravity through the effect of pressure broadening. It also de-

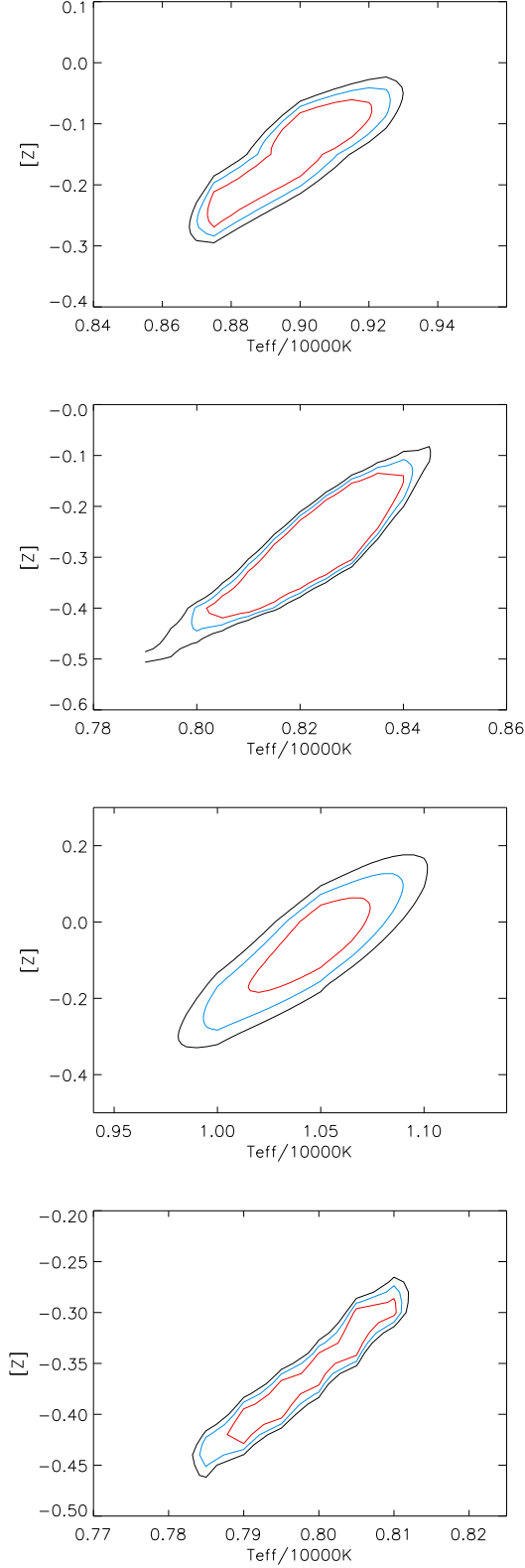


FIG. 7.— Isocontours $\Delta\chi^2$ for targets Slit 1 (top left), Slit 14 (top right), Slit 16 (bottom left), Slit 17 (bottom right). $\Delta\chi^2=3$ (red), 6 (blue), 9 (black).

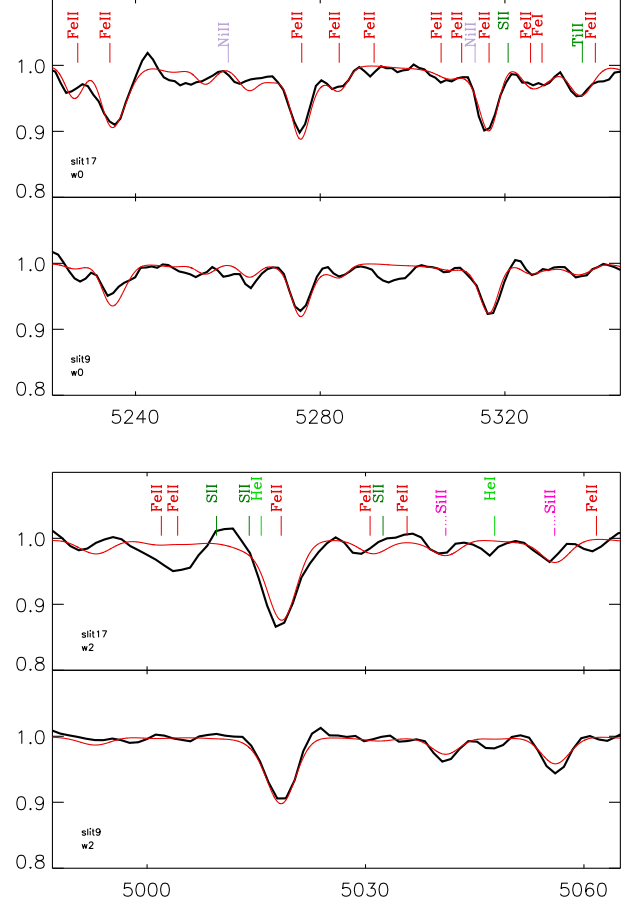


FIG. 8.— Observed metal line spectra (black) of targets Slit 17 and 9 in spectral windows 0 and 2 compared with the model calculations (red) obtained for the final stellar parameters of Table 3.

depends on temperature through the excitation of the first excited level of the hydrogen atom. As the result, fits of equal quality as shown in Figure 2 can be obtained at different values of T_{eff} for different gravity $\log g$. At lower T_{eff} the $\log g$ fit-values are lower, while they are higher at higher T_{eff} . This defines a fit curve in the $(\log g, T_{\text{eff}})$ -plane along which the calculated Balmer lines agree with the observations. An example is shown in Figure 3 for Slit 9. The uncertainty of this fit curve is given by the 0.05 dex uncertainty of the $\log g$ fit at a fixed temperature. We note that the fit of the Balmer lines is practically independent of assumptions on stellar metallicity. Thus, the fit of the Balmer lines provides already a strong restriction of the possible values for T_{eff} and $\log g$. Figure 4 and 5 show examples of Balmer line fits for the remaining targets.

In the next step, we use the spectrum of the observed metal lines to determine effective temperature and metallicity. As in our previous work, we define metallicity as $[Z]=\log Z/Z_{\odot}$, where Z_{\odot} is the solar metallicity. We then move along the Balmer line fit curve in the $(\log g, T_{\text{eff}})$ -plane as, for instance, in Figure 3 and compare at each T_{eff} the observed spectrum with synthetic spectra calculated for different $[Z]$ ranging from $[Z] = -1.30$ to 0.5. For the comparison, we define nine spectral windows with metal and helium lines (see Figures 8, 9 and 10). We split the observed spectrum into different spectral windows to allow for a piecewise accurate continuum normalization. The choice of the windows also avoids

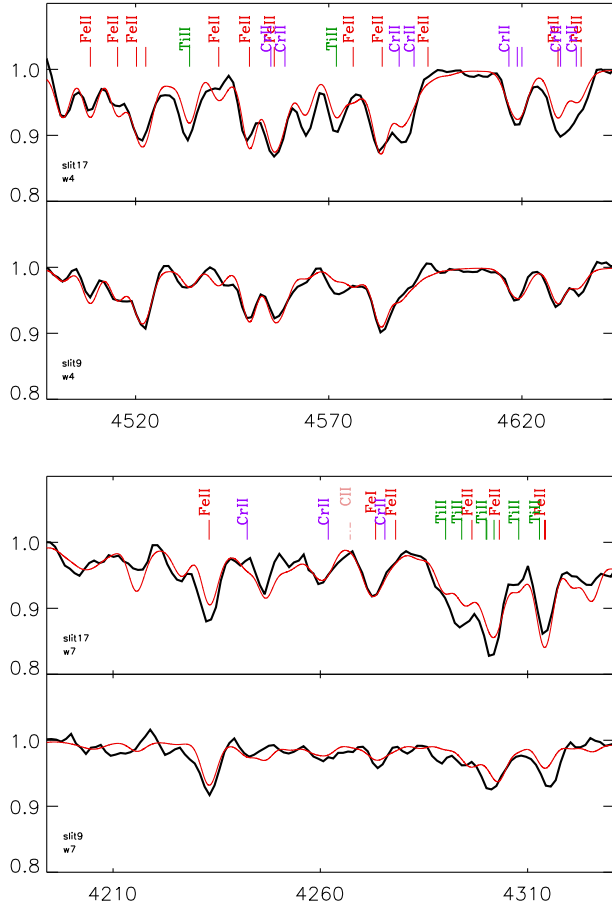


FIG. 9.— Same as Figure 8 but for spectral windows 4 and 7, respectively.

the Balmer lines and nebular emission lines. Sometimes we encounter flaws in some of the observed spectral windows. In such cases, the window is not used for the analysis. For each temperature T_{eff} and metallicity $[Z]$ we then calculate a χ^2 -value

$$\chi^2([Z], T_{\text{eff}}) = (S/N)^2 \sum_{j=1}^{n_{\text{pix}}} (F_j^{\text{obs}} - F([Z], T_{\text{eff}})_j^{\text{calc}})^2 \quad (1)$$

where S/N is the average target signal-to-noise ratio as given in Table 1. The sum is extended over all spectral windows and n_{pix} is the sum of all wavelength points in all spectral windows. The $\chi^2([Z], T_{\text{eff}})$ -table obtained in this way allows us to determine the minimum χ_{min}^2 in the $([Z], T_{\text{eff}})$ -plane and to calculate $\Delta\chi^2$ isocontours around this minimum. In order to assess which isocontour corresponds to a $1\text{-}\sigma$ uncertainty in this two-dimensional χ^2 minimalization process we carry out extensive Monte Carlo calculations to simulate the fitting process. For each target we simulate 1000 observed spectra by superimposing model spectra with Gaussian Monte Carlo noise corresponding to the observed S/N -ratio of our targets. For each simulated spectrum we calculate $\chi^2([Z], T_{\text{eff}})$ -tables exactly in the same way as for the observed spectrum and determine minima χ_{min}^2 in the $([Z], T_{\text{eff}})$ -plane. We compare the distribution of these minima in the $([Z], T_{\text{eff}})$ -plane with iso-

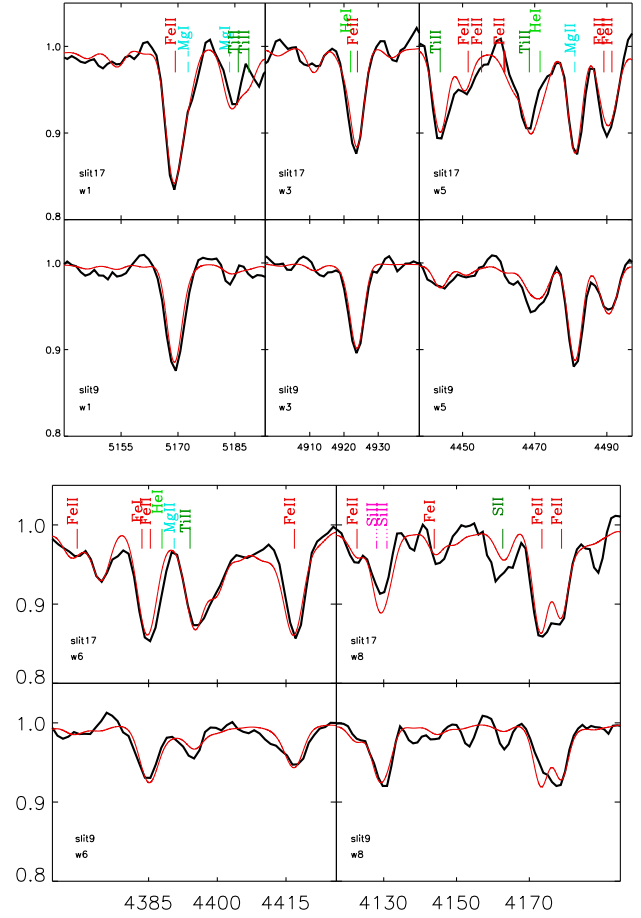


FIG. 10.— Same as Figure 8 but for spectral windows 1, 3, 5 and 6, 8, respectively.

contours calculated from the average of the χ^2 -tables over all 1000 simulations to determine which $\Delta\chi^2$ isocontour encloses 68% of the MC solutions obtained ($\Delta\chi^2$ is the increment relative to the χ_{min}^2 value found for the averaged χ^2 -table). For all targets we find that $\Delta\chi^2 = 3$ is a conservative estimate in reasonable agreement with statistical theory (Press et al. 2007). More details describing the whole analysis process can be found in Hosek et al. (2014).

Figure 6 shows the isocontours obtained in this way for target Slit 9 indicating an effective temperature of $T_{\text{eff}} = 8750^{+150}_{-250}$ K and a metallicity $[Z] = -0.30 \pm 0.10$. The gravity at this central fit point is $\log g = 1.00 \pm 0.05$ (see again Figure 3 as a reference to the $\log g$ fit of the Balmer lines). Figure 7 displays similar isocontour fits for targets Slit 1, 14, 16 and 17 providing well constrained values for T_{eff} , $[Z]$ and gravity $\log g$ as summarized in Table 2. For illustration of the final metal line fits, Figures 8, 9 and 10 show the comparison of the observed spectra of Slit 9 and 17 in all nine spectral windows with models calculated for final stellar parameters given in Table 2.

Some of the spectral windows selected also contain a contribution of He I lines, thus, the metallicity and temperature obtained depends also on the helium abundance adopted (we use helium abundances as generally found in high resolution, high signal-to-noise-studies of BSGs, see Hosek et al., 2014). However, for targets Slit 1, 9, 14, and 17 the helium lines

are weak and have no influence on the final result. For Slit 16 there is a weak dependence on helium abundance, but the effect is small compared to the uncertainties encountered for this target. Target Slit 3 has an earlier spectral type and the He I lines are the strongest lines. As a consequence, at the S/N of this target metallicity is not well constrained and we can only use the He I lines for a relatively uncertain estimate of effective temperature. We will use this target only for the distance determination using the flux weighted gravity $\log g_F = \log g - 4 \log T_{\text{eff}}/10^4 \text{K}$ (see sections 4 and 7). Luckily, the large uncertainty in T_{eff} does not affect the precision with which $\log g_F$ can be determined, because for effective temperatures larger than 10000K the strength of the Balmer lines is constant with constant $\log g_F$ for a large range of T_{eff} (see (Kudritzki et al. 2008), section 6.1 for a physical explanation of this effect). This means that even while one needs higher (lower) gravities at higher (lower) temperatures than in in Figure 5 to fit the Balmer lines of Slit 3, $\log g_F$ will be the same and is determined accurate to 0.05 dex. Thus, while not useful as a metallicity indicator Slit 3 can still be used for the distance determination.

4. REDDENING AND STELLAR PROPERTIES

With stellar effective temperatures and gravities obtained from the spectroscopic analysis and summarized in Table 2 we can discuss the stellar properties and evolutionary status of the BSGs observed. Figure 11 (top) shows the location of the target stars in the $(T_{\text{eff}}, \log g)$ -diagram compared with evolutionary tracks. The advantage of $(T_{\text{eff}}, \log g)$ -diagram is that it is independent of assumption on the distances. This allows to investigate the properties of the stellar objects studied without being affected by distance uncertainties. The NGC 3621 BSG targets form an evolutionary sequence of stars, which originally had masses about $25 M_{\odot}$ and which have now evolved away from the main sequence. Three of the objects seem to be somewhat more massive than $25 M_{\odot}$ although the uncertainties in $\log g$ do not allow for a clear conclusion. A distance independent alternative to the $(T_{\text{eff}}, \log g)$ -diagram is the spectroscopic Hertzsprung-Russell diagram (sHRD), which has been recently introduced and discussed by Langer & Kudritzki (2014). This diagram shows the inverse of the flux weighted gravity (as defined in section 3) versus effective temperature and is morphologically very similar to the classical HRD. The advantage of this way to study stellar evolution is that flux weighted gravities can usually be determined with higher precision than gravities (see Kudritzki et al., 2008, section 6, for a detailed discussion). Figure 11 (middle) displays this diagram with the NGC 3621 BSGs compared to evolutionary tracks. We see a clear indication that at least one of the targets is more massive than $25 M_{\odot}$.

A direct determination of stellar masses, radii and luminosities requires the knowledge of reddening, extinction and distance. With the stellar atmospheric parameters T_{eff} , $\log g$ and $[Z]$ of Table 2 we calculate model atmospheres colors B-V and V-I. Comparison with the observed colors of Table 1 yields reddening $E(B-V)$ directly from B-V, but also from V-I assuming $E(B-V)=0.78E(V-I)$. The average of these two values is given in Table 2. The uncertainty is 0.03 mag in agreement with the estimated uncertainty of the HST photometry. Assuming $R_V=3.2$ for the ratio extinction A_V to reddening $E(B-V)$ we can then calculate de-reddened magnitudes. Adding the bolometric correction obtained from the model atmosphere calculation gives the de-reddened apparent

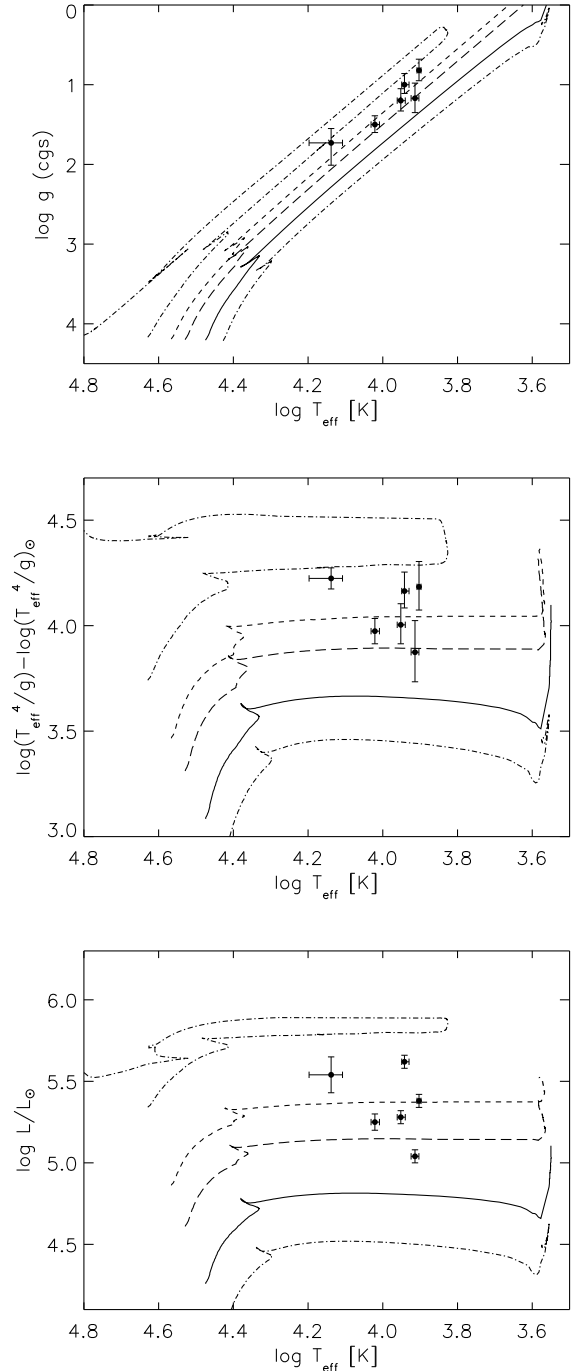


FIG. 11.— Stellar parameters of the observed NGC 3621 BSGs compared with evolution tracks (with 12, 15, 20, 25, 40 M_{\odot} , respectively) including the effects of rotational mixing (Meynet & Maeder 2005). Top: $(T_{\text{eff}}, \log g)$ -diagram. Middle: sHRD diagram. Bottom: HRD diagram.

bolometric magnitudes of Table 2.

The average reddening found for the six targets is $\langle E(B-V) \rangle = 0.18$ mag with only a small dispersion of 0.02 mag. This is larger than the foreground reddening of 0.07 or 0.08 mag measured by Schlafly & Finkbeiner (2011) and Schlegel et al. (1998), respectively, but smaller than the value of 0.28 mag found by Freedman et al. (2001) in the HST key project study of Cepheids. Bresolin et al. (2012) using the H II region

TABLE 2
STELLAR PARAMETERS

name	T_{eff} K	log g cgs	log g_F cgs	[Z] dex	E(B-V) mag	BC mag	m_{bol} mag
(1)	(2)	(3)	(4)	(5)	(6)	(7)	(8)
Slit 1	8950_{250}^{200}	$1.20_{0.15}^{0.13}$	$1.39_{0.10}^{0.09}$	$-0.15_{0.12}^{0.12}$	0.19	-0.11	20.61 ± 0.10
Slit 3 ^a	13750_{1000}^{2000}	$1.73_{0.18}^{0.28}$	$1.17_{0.05}^{0.05}$		0.19	-0.99	19.98 ± 0.28
Slit 9	8750_{250}^{150}	$1.00_{0.14}^{0.11}$	$1.23_{0.09}^{0.08}$	$-0.30_{0.10}^{0.10}$	0.17	-0.09	19.77 ± 0.10
Slit 14	8200_{200}^{200}	$1.17_{0.19}^{0.18}$	$1.52_{0.15}^{0.14}$	$-0.30_{0.10}^{0.15}$	0.22	0.04	21.21 ± 0.10
Slit 16	10500_{300}^{250}	$1.50_{0.11}^{0.10}$	$1.42_{0.06}^{0.06}$	$-0.10_{0.10}^{0.15}$	0.17	-0.37	20.69 ± 0.13
Slit 17	8000_{100}^{100}	$0.82_{0.14}^{0.13}$	$1.21_{0.12}^{0.11}$	$-0.35_{0.10}^{0.10}$	0.18	0.06	20.34 ± 0.10

^a T_{eff} estimated from He lines; no metallicity determined

Balmer decrements detected a large range of extinction between 0.0 to 0.5 mag depending on the location within the galaxy. The BSGs of our study (see BKMP, Figure 1) are not located in areas where Bresolin et al. (2012) observed larger extinction (see their Figure 3). They were selected because of their relatively blue colors and brightness, which may have introduced a bias towards lower reddening. We, thus, conclude that our extinction values are not in disagreement with their results. Most importantly, we find that targets Slit 9, 17, and 16 at $R/R_{25} = 1.29, 0.98$ and 0.91 , respectively, have reddening values of 0.17 mag. This confirms the conclusion by Bresolin et al. (2012) that the outer disk of NGC 3621 is not dust free.

In section 7, we will use the flux-weighted gravity - luminosity relationship (FGLR) to determine a distance modulus to NGC 3621 of $\mu = 29.07 \pm 0.1$ mag. With this distance modulus we obtain the absolute magnitudes and luminosities given in Table 3. The bottom of Figure 11 then shows the classical Hertzsprung-Russell diagram (HRD) of the BSGs in NGC 3621 compared with evolutionary tracks. Generally, including the additional information obtained from the distance does not change the conclusion about evolutionary status and stellar masses except for the target with the lowest T_{eff} , Slit 17. Here the location in HRD indicates a lower mass than one would derive from sHRD. We will investigate this further by looking at the directly determined stellar masses.

There are two ways to determine stellar masses. We can derive stellar radii from the luminosities and effective temperatures and then use the gravities to calculate spectroscopic masses. Alternatively, we can use the stellar luminosities and compare with the luminosities and the actual masses of the evolutionary tracks at the BSG temperatures to derive evolutionary masses (see Kudritzki et al. 2008 for details). Both mass estimates are given in Table 3. Because of the relatively large uncertainties of stellar gravities compared with the uncertainties of effective temperature and photometry which affect the stellar luminosity, the uncertainties of the spectroscopic masses are larger than those of the evolutionary masses. However, it is important to note that the latter do not account for possible systematic uncertainties of the evolutionary tracks caused, for instance, by the approximate treatment of rotationally induced mixing or the effects of mass-loss.

In Figure 12 we compare the NGC 3621 BSG luminosities and spectroscopic masses with the mass-luminosity relationship of stellar evolution theory. On average, there is agreement between theory and observations with an indication that most of the objects are slightly overluminous similar

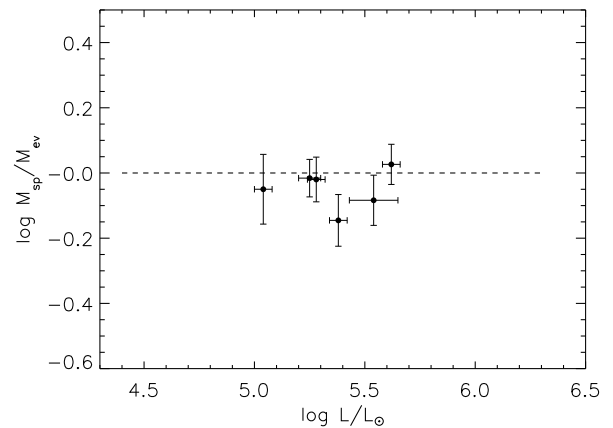
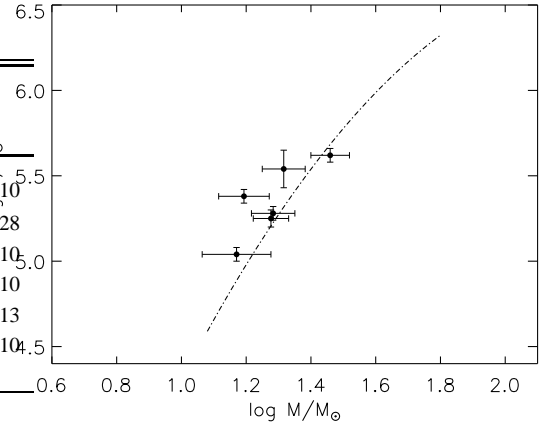


FIG. 12.— Discussion of BSG stellar masses in NGC 3621. Top: Observed mass-luminosity relationship compared with stellar evolution theory using the tracks of Figure 11. Bottom: Logarithm of the ratio of spectroscopic to evolutionary masses as a function of luminosity.

TABLE 3
ABSOLUTE MAGNITUDES, LUMINOSITIES, RADII AND MASSES

name	M_V mag	M_{bol} mag	log L/L_{\odot} dex	R R_{\odot}	M_{spec} M_{\odot}	M_{evol} M_{\odot}
(1)	(2)	(3)	(4)	(5)	(6)	(7)
Slit 1	-8.35	-8.46	5.28 ± 0.04	128.8 ± 9.1	19.2 ± 3.2	20.1 ± 0.7
Slit 3	-8.10	-9.09	5.54 ± 0.11	103.7 ± 27.2	20.7 ± 3.4	25.1 ± 2.4
Slit 9	-9.21	-9.30	5.62 ± 0.04	281.6 ± 18.9	28.8 ± 4.2	27.1 ± 1.0
Slit 14	-7.90	-7.86	5.04 ± 0.04	165.0 ± 11.4	14.8 ± 4.1	16.6 ± 0.5
Slit 16	-8.01	-8.38	5.25 ± 0.05	128.3 ± 10.6	18.9 ± 2.5	19.6 ± 0.8
Slit 17	-8.75	-8.69	5.38 ± 0.04	254.7 ± 13.5	15.6 ± 3.1	21.8 ± 0.7

to what has been found in previous studies. The most extreme case is Slit 17 as already indicated by the comparison of the sHRD and HRD. This conclusion is confirmed by the plot of the ratio of spectroscopic to evolutionary masses also shown in Figure 12. On average spectroscopy masses are lower by 0.05 dex. This is a similar difference as already encountered in the previous extragalactic studies of BSGs (Kudritzki et al. 2008, U et al. 2009, Kudritzki et al. 2012, Hosek et al. 2014). It is not clear whether this indicates a systematic deficiency

of the spectroscopic $\log g$ diagnostics or the evolutionary tracks used to construct the evolutionary mass-luminosity relationship. The discrepancy in the case of Slit 17 (0.145 dex or 28%) seems to be more significant. We note that Slit 17 with its stellar parameters is at the low temperature, low gravity edge of our model atmosphere grid, where according to Przybilla et al. (2006) pressure inversions are encountered in the model atmosphere structure, which may artificially weaken the Balmer lines in the model spectra. However, the pressure inversions in the models used for Slit 17 are only marginal and much smaller than for the $T_{\text{eff}}=7700\text{K}$ model discussed by Przybilla et al. In consequence, no suspicious changes in the strengths of calculated spectral lines as a function of gravity (for fixed effective temperature) are found. We, thus, conclude that mass-loss processes not included in the evolutionary calculations such as non-conservative binary evolution or evolution back to hotter temperature from the red supergiant stage are a more likely reason for the discrepancy.

5. METALLICITY AND CHEMICAL EVOLUTION OF THE EXTENDED DISK OF NGC 3621

The H II region emission line study by Bresolin et al. (2012) of the disk of NGC 3621 found a significant oxygen abundance gradient from the center of the galaxy to galactocentric distances of $R/R_{25} \approx 0.8$ corresponding to ≈ 7 kpc. Further out the oxygen abundance profile became flat and stayed constant until $R/R_{25} \approx 2.0$ (18 kpc). The result of this work is displayed in Figure 13 and shows that the oxygen abundances based on the use of the strong emission lines (strong line methods) depend heavily on the calibration used. The N2 calibration gives values about 0.4 dex lower than the R_{23} calibration (see Bresolin et al. 2012 for details). A more accurate method for H II regions is the use of the forbidden [O III] $\lambda 4363$ auroral lines which can be used to constrain the H II region electron temperatures. To detect and accurately measure the flux of this rather weak emission line requires long exposure times. Bresolin et al. (2012) were able to detect [O III] $\lambda 4363$ in twelve H II regions mostly at large galactocentric distances and at low oxygen abundances. This is very likely a selection effect since at low metallicities H II regions are hotter, which increases the [O III] $\lambda 4363$ emission. The oxygen abundances obtained with the help of the auroral $\lambda 4363$ line support the N2 calibration which gives lower abundances.

The spectroscopy of the NGC 3621 BSGs now allows for the first time to compare directly determined stellar metallicities of the young stellar population with the H II oxygen abundances in the outer disk of this galaxies. This is done in Figure 13. The first conclusion is that the BSG metallicities are significantly smaller than those obtained from the R_{23} strong line calibration but larger than those obtained from N2. They are also somewhat larger than the more accurate metallicities based on the use of [O III] $\lambda 4363$. The difference is small, only ≈ 0.1 dex, but appears to be systematic. This could be due to systematic effects influencing the [O III] $\lambda 4363$ method. For instance, the depletion of interstellar medium oxygen into interstellar dust could lead to a depletion of ISM oxygen abundance relative to stellar metallicity. We note that Peimbert & Peimbert (2010) estimate H II region dust depletion factors for oxygen of the order of 0.1 dex, just the same order of magnitude as encountered here. As another possibility the bias of [O III] $\lambda 4363$ detection towards lower metallicity as mentioned above could affect the comparison (see also Zurita & Bresolin 2012 for a discussion). Of course,

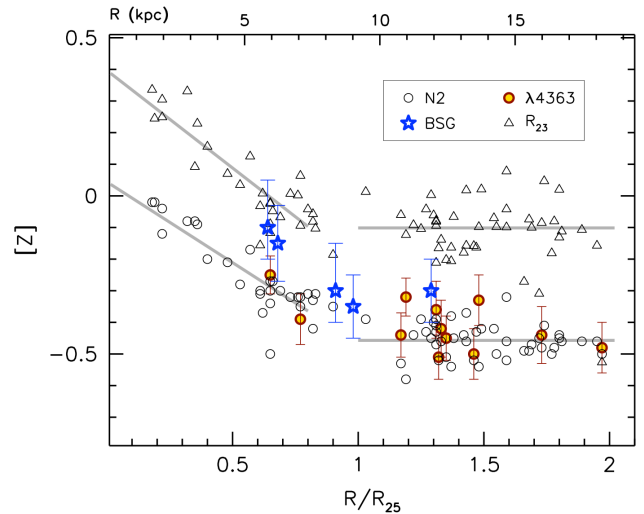


FIG. 13.— Metallicity in NGC 3621 as a function of galactocentric radius (R/R_{25} on the bottom scale and kpc on the top scale). Blue supergiant metallicities $[Z] = \log Z/Z_{\odot}$ obtained from the spectral analysis described in section 3 are plotted as blue stars. Open black circles, triangles and yellow filled red circles represent oxygen abundances as measured by Bresolin et al. (2012). The transformation of H II oxygen abundances $N(\text{O})/N(\text{H})$ to $[Z]$ is given by $[Z] = [\text{O}/\text{H}] - [\text{O}/\text{H}]_{\odot}$, where $[\text{O}/\text{H}] = 12 + \log(N(\text{O})/N(\text{H}))$ and $[\text{O}/\text{H}]_{\odot} = 8.69$ (Asplund et al. 2009). The values of the open black circles and triangles are from the same H II regions but use strong emission lines and different calibrations (N2 or R_{23}). The values of the yellow filled red circles are from the subset of H II regions, where the auroral line [O III] $\lambda 4363$ was detected. The grey linear curves are regressions for the abundances from the strong line N2 and R_{23} calibrations split into an inner and an outer part.

also the BSG metallicity determination could be systematically affected, although the high resolution, high S/N studies by Przybilla et al. (2006) indicate that such systematic effects are probably small. It is also important to note that the BSG metallicities are based on a fit of the entire metal line spectrum (see Figures 8, 9 and 10) and are, thus, mostly representing the abundances of iron and to a weaker extend those of chromium and some higher α -elements such as magnesium, silicon and titanium. In this sense a deviation of the ratio of oxygen to iron abundance caused by a chemical evolution history in the extended disk of NGC 3621 different from the solar neighborhood can also not be ruled out. Recent work on Local Group dwarf galaxies (Tolstoy et al. 2009, Hosek et al. 2014) indicates that such deviations might exist.

Independent of the small discrepancy encountered the quantitative spectroscopy of BSGs as a new and independent tool to investigate the metallicity of the young stellar population in NGC 3621 clearly strengthens the conclusions by Bresolin et al. (2012). The BSG metallicities confirm the transition from a metallicity gradient in the inner disk to constant metallicity in the outer disk. With $[Z] \approx -0.3$ obtained for the BSGs the metallicity in the outer extended disk of NGC 3621 is much higher than expected. Bigiel et al. (2010) have studied the radial profiles of star formation rate and neutral hydrogen gas column density in a larger sample of spiral galaxies and concluded that star formation in the outer disks is proceeding very inefficiently. In the case of NGC 3621 they measured $\Sigma_{\text{SFR}} = 10^{-10} M_{\odot} \text{ yr}^{-1} \text{ pc}^{-2}$ for the star formation rate column density and $\Sigma_{\text{HI}} = 5 M_{\odot} \text{ pc}^{-2}$ for the H I column density at a galactocentric distance of $R/R_{25} = 1.0$. Assuming that the outer disks have been originally formed out of very metal poor pristine gas we use a simple 1-zone (“closed box”) chemical evolution model (see ,

for instance, Pagel 2009, page 251) and relate the metallicity mass fraction $Z_{mass}(t)$ of the ISM and the young stellar population at time t after the formation of the outer extended disk to $M_{stars}(t)$ and $M_{gas}(t)$, the masses confined in stars and ISM gas, respectively

$$Z_{mass}(t) = y_Z \ln(1 + M_{stars}(t)/M_{gas}(t)). \quad (2)$$

y_Z is the metallicity yield, i.e. the fraction of metals returned to the ISM per newly formed stellar mass. We adopt a value of y_Z equal to $Z_{mass,\odot} = 0.014$, the metallicity mass fraction of the sun (Asplund et al. 2009, estimates of metallicity yields are discussed by Maeder 1992, Zoccali et al. 2003 and Pagel 2009). Under the additional simplifying assumption that the presently observed rate is representative for the star formation process since the outer disk has formed and that the number ratio of helium to hydrogen in the ISM is 0.1 we can approximate

$$M_{stars}(t)/M_{gas}(t) = \Sigma_{SFRT}/(1.4\Sigma_{HI}) = \frac{1}{70}t_{Gyr} \quad (3)$$

with t_{Gyr} the age of the outer disk in Gyr.

Eq. (1) then allows us to calculate the time required to build up the presently observed metallicity of $[Z] \approx -0.3$ corresponding to $Z_{mass} = 0.5Z_{mass,\odot}$ through in situ chemical evolution with the presently observed rate of star formation. We obtain 45 Gyr, much larger than Hubble time. (We note that this value is larger than the 10 Gyr estimated by Bresolin et al. (2012). The difference is caused by the use of the ‘‘closed box’’ relationship of eq. (2) rather than eq. (1) of Bresolin et al., the 0.1 dex higher metallicity, the use of $1.4M_{HI}$ to represent M_{gas} and a metallicity yield reflecting the lower solar metallicity of Asplund et al. 2009). As an estimate of the uncertainties, by doubling the star formation rate and simultaneously reducing $[Z]$ to -0.4 we obtain 17 Gyr still larger than Hubble time.

Bresolin et al. (2012) summarize the compelling evidence from cosmological simulations and observations that the outer disks of spiral galaxies have ages around 5 Gyr. For such an age eq. (2) predicts a metallicity of $[Z] = -1.1$ much lower than observed. This confirms their conclusion that in situ star formation is unlikely to having produced the metallicity of the young stellar population in the outer extended disk and that additional mechanisms are needed. Ejection of chemical enriched gas from central galactic regions and subsequent accretion onto the outer disk is discussed by Bresolin et al. (2012) as the most promising mechanism.

6. DISTANCE

The spectroscopically determined temperatures and gravities of the BSGs together with the individual reddening corrections of the photometry can be used to determine a distance to NGC 3621 using the flux-weighted gravity–luminosity relationship (FGLR). This new distance determination method was introduced by Kudritzki et al. (2003) and Kudritzki et al. (2008). It relates the flux-weighted gravity ($g_F \equiv g/T_{eff}^4$, T_{eff} in units of $10^4 K$) of BSGs to their absolute bolometric magnitude M_{bol}

$$M_{bol} = a(\log g_F - 1.5) + b \quad (4)$$

with $a = 3.41 \pm 0.16$ and $b = -8.02 \pm 0.04$ as determined by Kudritzki et al. (2008). The physical background of the FGLR is that massive stars after they leave the main sequence

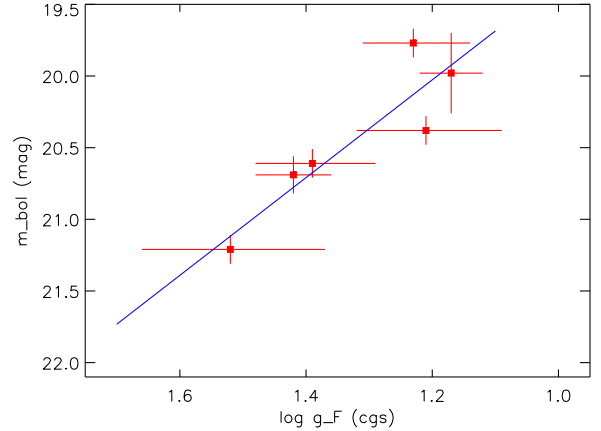


FIG. 14.— Flux weighted Gravity - luminosity relationship (FGLR) of the BSGs observed in NGC 3621. Plotted is the dereddened apparent bolometric magnitude versus flux-weighted gravity of the individual BSGs (red). The blue linear curve is the FGLR of eq. (2) shifted by a distance modulus $\mu = 29.07$ mag.

evolve at constant mass and luminosity across the HRD. In consequence, because of $g_F \propto M/L$ the flux-weighted gravity remains constant during the horizontal HRD evolution and is independent of temperature. On the other hand, the luminosity increases strongly with stellar mass and, therefore, g_F decreases with luminosity. This establishes the FGLR. So far, distance determinations using the FGLR have already been carried for a number of galaxies (see Kudritzki et al. 2012 and Hosek et al. 2014 and references, therein).

To determine the distance to NGC 3621 we use apparent the bolometric magnitudes m_{bol} and flux-weighted gravities $\log g_F$ and fit a regression of the form

$$m_{bol} = a(\log g_F - 1.5) + b_{NGC3621}. \quad (5)$$

Since we have only six objects for our regression over a limited range of $\log g_F$, we adopt the slope of the FGLR of eq. (4) and fit only the intercept $b_{NGC3621}$. The result is shown in figure 14, which indicates that there is a clear relationship between flux-weighted gravity and bolometric magnitude well represented by eq. (5). The scatter is $\sigma = 0.225$ mag. The difference between the fitted intercept $b_{NGC3621}$ and the intercept b of the calibration relation eq. (4) yields the distance modulus $\mu = 29.07 \pm 0.09$ mag, where the uncertainty is given by $\sigma/\sqrt{6}$. The uncertainty caused by the errors of a and b (see above) is 0.06 mag.

We compare this result with published Cepheid distances. During the HST Key Project on the extragalactic distance scale 69 cepheids have been detected in NGC 3621 (Rawson et al. 1997). Using their period luminosity relationship (PLR) observed in multiple photometric passbands and comparing to the LMC as the distance scale anchor point Freedman et al. (2001) determined a distance modulus of $\mu = 29.08 \pm 0.06$ mag. Kanbur et al. (2003) used the same data set but an improved LMC PLR based on OGLE observations and corrected for charge transfer effects (CTE) in the HST camera to obtain a slightly larger distance modulus of 29.15 ± 0.06 mag. Both distance moduli quoted were obtained for the case assuming that the Cepheid PLR does not vary with metallicity, but in both papers a metallicity correction was also applied yielding distance moduli 0.03 and 0.05 mag larger. We note, however, that the metallicity corrections are very uncertain for

a variety of reasons (see Kudritzki et al., 2012, 2013 for a discussion). Patreul et al. (2002) used a HIPPARCOS based calibration of Milky Way Cepheids for the PLR and obtained $\mu = 29.13 \pm 0.06$ mag. Kanbur et al. (2003) also included a distance determination based on an alternative Milky way PLR calibration of yielding $\mu = 29.22 \pm 0.06$ mag. It seems that within the range of uncertainties the distance obtained with the new BSG FGLR method is in good agreement with the HST Cepheid work.

An alternative method to obtain distances is the use of the magnitude of the observed tip of the red giant branch (TRGB). The earlier work by Sakai et al. (2004) and Rizzi et al. (2007) resulted in relatively large distance moduli, 29.36 ± 0.11 mag and 29.26 ± 0.12 mag, respectively. However, the most recent work published in the EDD database (<http://edd.ifa.hawaii.edu>, see Tully et al. 2009 for a description) provides a distance $\mu = 29.11 \pm_{0.04}^{0.06}$ mag in good agreement with our FGLR result and the Cepheid studies.

7. DISCUSSION AND CONCLUSIONS

The spectroscopic study presented in work this provides the first direct information about the chemical composition of the young stellar population in the disk of the spiral galaxy NGC 3621. We observe the transition from an inner disk with a metallicity gradient to an outer disk with constant metallicity. This confirms the result by Bresolin et al. (2012) obtained from their extensive study of H II regions. The BSG in the outer extended disks are reddened by ~ 0.17 mag indicating

a significant amount of interstellar dust. Their metallicity is only a factor of two lower than the metallicity of the sun. This is a factor of six higher than one would expect from in situ chemical evolution at the present level of star formation and neutral hydrogen density over the lifetime of the extended disk of 4-6 Gyr predicted by cosmological simulations. To produce such a high metallicity under these conditions would require 45 Gyr much longer than Hubble time. This requires additional mechanisms to build up the high level of metallicity observed. One possible mechanism suggested by cosmological simulations is the the ejection of metal enriched gas from the inner disk through galactic winds and subsequent accretion in the outer disk.

Using stellar temperatures, gravities and reddening corrected photometry of the individual the individual BSGs as obtained from the quantitative spectroscopic analysis a distance to NGC 3621 of $D = 6.52 \pm 0.28$ Mpc is obtained. This distance is in good agreement with Cepheid distance determinations based on the sample of cepheids detected by the HST Key Project on the extragalactic distance scale. It also agrees with a most recent determination using NGC 3621 HST color magnitude diagrams and the tip of the red giant branch.

This work was supported by the National Science Foundation under grant AST-1008798 to RPK and FB.

Facilities: ESO VLT (FORs), HST (ACS).

REFERENCES

- Asplund, M., Grevesse, N., Sauval, A. J., & Scott, P. 2009, *ARA&A*, 47, 481
 Bigiel, F., Leroy, A., Walter, F., et al. 2010, *AJ*, 140, 1194
 Bresolin, F., Kudritzki, R.-P., Mendez, R. H., & Przybilla, N. 2001, *ApJ*, 548, L159
 Bresolin, F., Schaerer, D., González Delgado, R. M., & Stasińska, G. 2005, *A&A*, 404, 1679
 Bresolin, F., Pietrzyński, G., Urbaneja, M. A., et al. 2006, *ApJ*, 648, 1007
 Bresolin, F., Urbaneja, M. A., Gieren, W., Pietrzyński, G., & Kudritzki, R.-P. 2007, *ApJ*, 671, 2028
 Bresolin, F., Gieren, W., Kudritzki, R.-P., et al. 2009, *ApJ*, 700, 309
 Bresolin, F., Ryan-Weber, E., Kennicutt, R. C., & Goddard, Q. 2009, *ApJ*, 695, 580
 Bresolin, F., Kennicutt, R. C., & Ryan-Weber, E. 2012, *ApJ*, 750, 122
 Bresolin, F. 2011, *ApJ*, 729, 56
 Castro, N., Urbanela, M. A., Herrero, A., et al. *A&A*, 542, 79
 Dalcanton, J. J., Williams, B. F., Seth, A. C., et al. 2009, *ApJS*, 183, 67
 de Blok, W. J. G., Walter, F., Brinks, E., et al. 2008, *AJ*, 136, 2648
 Dolphin, A. et al. 2002, *AJ*, 123, 3154
 Ercolano, B., Wesson, R., & Bastian, N. 2010, *MNRAS*, 401, 1375
 Evans, C. J., Howarth, I. D. 2003, *MNRAS*, 345, 431
 Evans, C. J., Bresolin, F., Urbaneja, M. A., et al. 2007, *ApJ*, 659, 1198
 Freedman, W. L., Madore, B. F., Gibson, B. K., et al. 2001, *ApJ*, 553, 47
 Goddard, Q., Bresolin, F., Kennicutt, R. C., Ryan-Weber, E., & Rosales-Ortega, F. F. 2011, *MNRAS*, 405, 2791
 Hosek Jr., M. W., Kudritzki, R. P., Bresolin et al., 2014, *ApJ*, in press (arXiv 1402.6358)
 Kanbur, S. M., Ngeow, C., Nikolaev, S., Tanvir, N. R., Hendry, M. A. 2003, *A&A*, 411, 361
 Kewley, L. J., & Ellison, S. L. 2008, *ApJ*, 681, 1183
 Koribalski, B. S., Staveland-Smith, L., Kilborn, V. A., et al. 2004, *AJ*, 128, 16
 Kudritzki, R. P., Urbaneja, M. A., Gazak, Z., et al. 2013, *ApJ*, 779, L20
 Kudritzki, R. P., Urbaneja, M. A., Gazak, Z., et al. 2012, *ApJ*, 747, 15
 Kudritzki, R. P., Urbaneja, M. A., Bresolin, F., et al. 2008, *ApJ*, 681, 269
 Kudritzki, R. P., Bresolin, F., & Przybilla, N. 2003, *ApJ*, 582, L83
 Langer, N., Kudritzki, R. P. 2014, *A&A*, in press (arXiv 1403.2212)
 Maeder, A. 1992, *A&A*, 264, 105
 Meynet, G. & Maeder, A. 2005, *A&A*, 429, 581
 Mould, J., & Sakai, S. 2008, *ApJ*, 686, L75
 Mould, J., & Sakai, S. 2009, *ApJ*, 697, 996
 Patreul, G., Teerikorpi, P., Theureau, G., Fouque, P., Musella, I., Terry, J. N. 2002, *A&A*, 389, 19
 Pagel, B. E. J. 2009, *Nucleosynthesis and Chemical Evolution of Galaxies*, second edition, Cambridge University Press
 Peimbert, A., & Peimbert, M. 2010, *ApJ*, 724, 791
 Press, W. H., Teukolsky, S. A., Vetterling, W. T., & Flannery, B. P. 2007, *Numerical Recipes: The Art of Scientific Computing*
 Przybilla, N., Butler, K., Becker, S. R., & Kudritzki, R. P. 2006, *A&A*, 445, 1099
 Rawson, D. M., et al. 1997, *ApJ*, 490, 517
 Rizzi, L., Tully, R. B., Makarov, D., et al. 2007, *ApJ*, 661, 815
 Saha, A., Thim, F., Tammann, G. A., et al. 2011, *ApJS*, 165, 108
 Sandage, A., Tammann, G. A., Saha, A., et al. 2011, *ApJ*, 653, 843
 Sakai, S., Ferrarese, L., Kennicutt, R. C., Jr., & Saha, A. 2004, *ApJ*, 608, 42
 Schlafly, E. F., Finkbeiner, D. P. 2011, *ApJ*, 737, 103
 Schlegel, D. J., Finkbeiner, D. P., & Davis, M. 1998, *ApJ*, 500, 525
 Stasińska, G., 2005 *A&A*, 434, 507
 Tolstoy, E., Hill, V., & Tosi, M. 2009, *ARA&A*, 47, 371
 Tully, R. B., Rizzi, L., Shaya, E. J., et al. 2009, *AJ*, 138, 323
 U, V., Urbaneja, M. A., Kudritzki, R.-P., et al. 2009, *ApJ*, 704, 1120
 Urbaneja, M. A., Kudritzki, R.-P., Bresolin, F., et al. 2008, *ApJ*, 684, 118
 Werk, J. K., Putman, M. E., Meurer, G. R., & Santiago-Figueroa, N. 2011, *ApJ*, 735, 71
 Zozzali, M., Renzini, A., Ortolani, S. et al. 2003, *A&A*, 399, 931
 Zurita, A., & Bresolin, F. 2012, *MNRAS*, 427, 1463